Feasibility Considerations on an Inkjet-Printed Capacitive Position Sensor for Electrostatically Actuated Resonant MEMS-Mirror Systems

Lisa-Marie Faller, *Student Member, IEEE*, and Hubert Zangl, *Member, IEEE*

***Abstract*— We present a systematic approach to enable an inkjet-printed capacitive position sensor for a resonant microelectromechanical systems (MEMS)-mirror system in a smart packaging solution. We adopt systematic noise analysis and employ a stochastic (Bayesian) estimator for position reconstruction. In this way, we exploit prior knowledge of the system and its dynamics. We can thus demonstrate a way to achieve very high position resolutions of $\text{res}_{\text{pos}} < 50$ nm. The considered arrangement is a part of a Michelson interferometer setup and, as such, subject to concise specifications regarding resolution and accuracy. The measurement system's analog front-end is designed in a carrier frequency setup. It enables a flexible choice of bandwidth and provides a measurement signal at a frequency well separated from that of the mirror actuation. The wide measurement range of $r_m = 1000$ μm, at an offset of $d_0 = 1000$ μm, and the high required position resolution of $\text{res}_{\text{pos}} < 50$ nm present major challenges for the inkjet-printed capacitive sensor. To overcome noise limitations inflicted by the measurement and system setups, and to enable nanometer resolution independently of the measurement bandwidth extended Kalman filtering as Bayesian approach to statistical signal processing is suggested. Noise analysis and stochastic position estimation are applied to the MEMS-mirror system. Evaluations demonstrate the high achievable resolutions using extended Kalman filtering. [2016-0275]**

***Index Terms*— Microelectromechanical systems (MEMS), capacitive sensing, electrostatic actuation, Fourier transform interferometry, extended Kalman filter, noise analysis.**

I. Introduction

MICRO-OPTICAL devices have gained vastly in interest over the last decade, and are, by now, deployed in various fields. Applications range from Fourier Transform InfraRed (FTIR) spectroscopy [1] and multimedia optical devices [2], [3] to light barriers [4]. Formerly, optical arrangements such as spectrometer devices, beamers, and others, used to consume a considerable amount of space. MicroElectroMechanical Systems (MEMS) now offer the possibility of integrating complex setups into mobile applications. Advanced MEMS products are also appropriate for the deployment in lab-on-chip systems for space missions or UAV-based analyses.

Among these optical systems employing MEMS, interferometers hold a prominent position. They provide a non-invasive and non-destructive method to chemically analyse liquid or solid probes of material. On the one hand, there already exist hand-held polychromator type devices exploiting wavelengths in the range of shortwave near-infrared to UV/Vis. On the other hand, spectrometers analysing the interaction of probes with mid-IR and longer wavelengths still suffer from deficiencies such as being bulky and expensive. Additionally, measurements may take up to several minutes. A major advantage of such spectrometers that exploit IR, is the straight forward detection of properties characteristic to the analytes, and their flexible applicability. Comparable other sensors employ a chemo- or bioreactive layer of material which alters properties when exposed to the analyte. Such principles come with the disadvantage of being mostly only sensitive to one substance and calibration is difficult.

Electrostatically driven microactuators, such as the ones considered here, are ideally suited for application in interferometer setups (compare [5]). Still, there are concise demands on the system performance: To keep the measurement time low and to provide a sufficient Signal to Noise Ratio (SNR) demands fast position tracking of the moving mirror. Furthermore, high position measurement accuracy is needed to add spectra congruently and to avoid smearing.

Existing devices are realized holding a reference interferometer to measure and control the mirror position [1], [6], [7] or at least feature optical position sensing [8]. While this optical feedback represents a fast and accurate way to measure the position, major drawbacks are its size and tight requirements regarding the diode mounting. Comparisons of interferometric and capacitive measurements on MEMS [9] have shown superior properties of the optical feedback in terms of device characterization, but such topologies do not usually fit into target package outlines [10]. A multilayer, inkjet-printed capacitive position sensor is considered to enable further miniaturization.

Capacitive sensing has proven to be applicable for nanometer position resolution (e.g. [11]) and offers beneficial properties with respect to costs, resolution and bandwidth [12]. The capacitive sensor will be manufactured as flat electrode structure. It then forms a parallel plate capacitor with the mirror plane, which is a common setup for nanometer applications [13]. The sensor is thus comparatively simpler to realize and integrate into an existing package than is the reference

Manuscript received November 9, 2016; revised January 31, 2017; accepted February 11, 2017. Date of publication March 15, 2017; date of current version May 31, 2017. This work was supported by the Competence Centers for Excellent Technologies (COMET) K1 Austrian Smart Systems Integration Research Center (ASSIC). The COMET Program is supported in part by the Austrian Federal Ministry for Transport, Innovation, and Technology (BMVIT); in part by the Austrian Federal Ministry of Science, Research, and Economy (BMWFW); and in part by the federal provinces of Carinthia and Styria. Subject Editor O. Solgaard.

The authors are with the Institute of Intelligent System Technologies, Alpen-Adria-Universität Klagenfurt, Klagenfurt 9020, Austria (e-mail: lisa-marie.faller@aau.at).

Color versions of one or more of the figures in this paper are available online at http://ieeexplore.ieee.org.

Digital Object Identifier 10.1109/JMEMS.2017.2672039

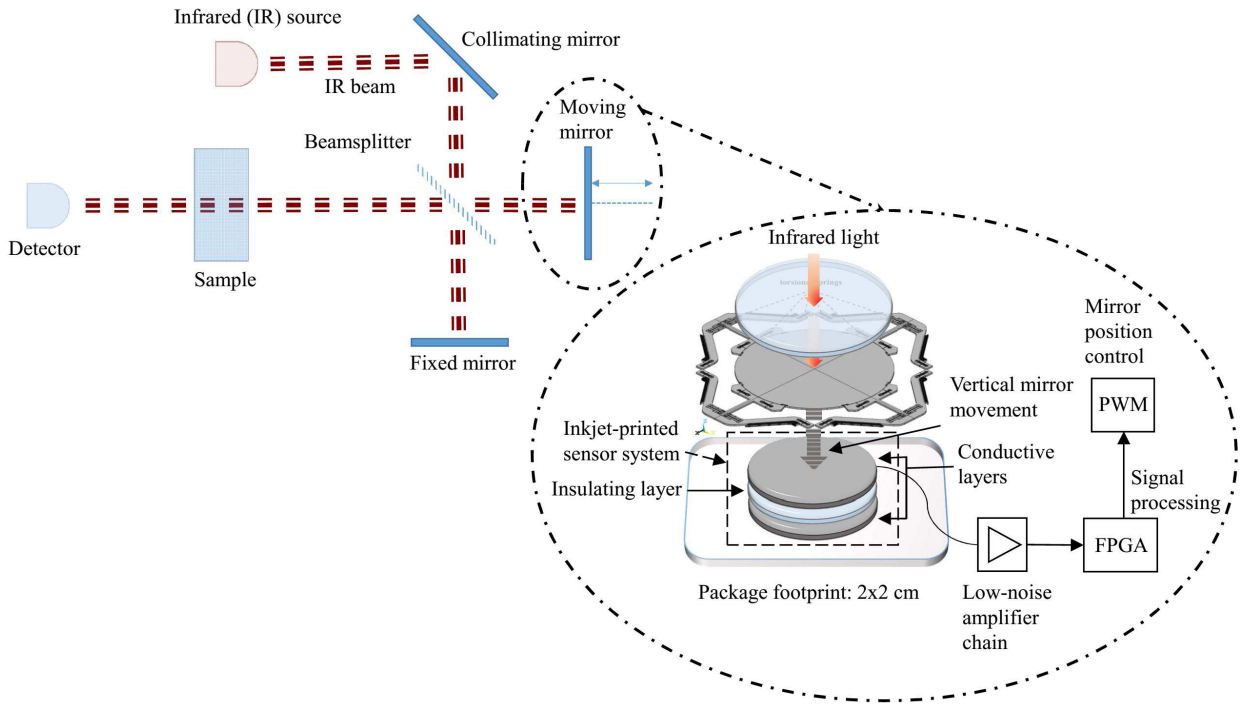

Fig. 1. The basic construction principle of a Michelson interferometer is schematically illustrated in the upper left. On the lower right, the suggested mirror position sensing system is shown. It is composed of a multilayer inkjet-printed capacitive sensor followed by a Low-Noise Amplifier (LNA) analog font-end and an FPGA. The FPGA is necessary for high speed digital signal processing and to provide the necessary trigger pulses for the Pulse Width Modulation (PWM) signal which drives the mirror.

interferometer setup. A capacitive sensor, manufactured by inkjet-printing (a rapid-prototyping technology), is further beneficial compared to other capacitive sensing approaches (e.g. [14], [15], [16]) since it enables individually adaptable designs and applicability to various setups. The sensor read-out is realized using a specifically designed measurement system. This measurement system is composed of an analog front-end which then feeds the sensor read-out to a high speed Field Programmable Gate Array (FPGA), i.e. the digital signal processing unit.

Considerations on the design of MEMS, subject to uncertainties [17], [18], as well as robust control of the electrostatic drive of MEMS [19] under parametric uncertainties can be found in literature. We extend these design methodologies by assessment of the possible lower bounds on the measurement uncertainties, to verify the sensor's suitability for nano-position tracking. This assessment is based on the stochastic system models, as part of the digital signal processing, which reflect the resonant sinusoidal mirror movement. In our work, we determine the Cramer Rao Lower Bound (CRLB) for the dynamic system parameters. We base our analysis on parametric models for the dynamic system as well as an Extended Kalman Filter (EKF). All of these system descriptions are likewise reconstructing the MEMS mirror position which is subject to systematic error and measurement noise. The overall system performance with regard to bandwidth and design restrictions can then be given together with a minimum bound on the achievable position measurement resolution. The suggested approach is applied to position reconstruction for a micromirror device.

In Sec. II, the interferometer and measurement system are described: In the first Subsec. II-A, the considered MEMS-mirror is introduced. The second Subsec. II-B, describes the capacitive sensor. Subsec. II-C elicits the setup of the analog front-end. In Subsec. II-D, noise analysis for the analog front-end follows. Afterwards, in Subsec. II-E, the sensor model is elaborated. In the last Subsec. II-F, the CRLB analysis for the parametric system description is presented. In Sec. III, the EKF is introduced, subsequently the system description as necessary for the algorithm is developed. Sec. IV gathers achieved results for the assessment of the algorithm's suitability for nano-position tracking based on the CRLB as well as effectively achievable position resolutions considering Additive White Gaussian Noise (AWGN) as well as systematic errors. These evaluations are done considering: firstly varying amplitudes of the mirror movement; and secondly, different sampling frequencies. Finally, a conclusion is provided in Sec. V.

II. Interferometer and Measurement System

A common way to manufacture an FTIR spectrometer device is a Michelson interferometer setup. The mechanism is composed of an IR source and two mirrors suspended in an angle of 90°, of which one is moveable (Fig. 1: upper left). The IR light beam is split and, through interference, distinct wavelengths of the IR light are selected, dependent on the moving mirror's position. The resulting monochromatic light beams pass through the sample of interest. Due to sample attributes at the molecular level, certain wavelengths are absorbed more than others. Thus, different intensities at distinct wavelengths are visible at the detector. After processing

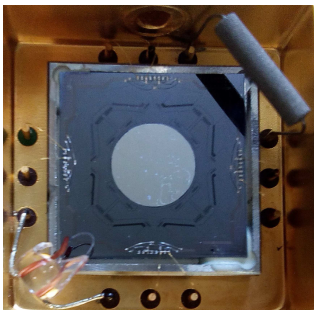

Fig. 2. MEMS-mirror (lighter circle in the middle) in vacuum package with vacuum sensor (lower left corner) and ion getter (upper right corner).

and Fourier transforming the data, a sample-characteristic spectrum can be seen. One movement, covering the full possible pathlength, the mirror can traverse, is called a scan. The so-called *mutliplex advantage* [20] characterizes this type of spectrometers: the devices' SNR can be increased by an increased number of scans (N) as SNR $\propto N^{\frac{1}{2}}$. On the other hand, this is equivalent to an increase of the measurement time. Additional crucial factors are: the congruency of added spectra (adding spectra non-congruently results in a smeared result-spectrum) and prevention of noise as this blurs peaks and could thus lead to miss-identification of substances. Consequently, a concise knowledge of the mirror position during each scan is crucial.

A. MEMS-Mirror

In this work, we address an electrostatically actuated micromirror (Fig. 2), which we also refer to as MEMS device or MEMS-mirror. The micromirror is designed in a CMOS compatible Silicon On Insulator (SOI) process. In [21] the considered MEMS is presented as piston device. The micromirror is suspended on four pantographs which are attached equally spaced to a circular mirror plate. The pantographs are designed to prevent mirror tilting, and suppress parasitic modes. The electrostatic drive is composed of in-plane electrodes, causing a translational mirror movement, perpendicular to the actuator plane. This type of movement is also referred to as piston mode. The mirror is driven by a Pulse Width Modulation (PWM) signal at twice the mirror resonance frequency, i.e. $f_{res} = 500$Hz and $f_{PWM} = 1000$Hz. The actuation control is laid out to guarantee for the largest possible mirror stroke, that is, to achieve the highest possible spectrometer resolution. The considered devices were reported to reach a spectral resolution of $res_{spec} = 25\text{cm}^{-1}$ at $d_{tr} = 200\mu$m translatory displacement with an acquisition time of $t_{aq} = 200\mu$s per scan [22], [6]. The uniformity and amplitude of the sinusoidal mirror-movement are dependent on environmental and external factors, i.e. temperature, ambient pressure and driving voltage. These factors, together with the high resolution requirements call for a precise in-depth system assessment, stating noise bounds and limitations. The assessment is done based on conservative presumptions.

While the presented methodology is generally applicable, an example is elaborated for a device which ideally moves at a resonance frequency of $f_m = 500$Hz and achieves a maximum stroke of $s_{max} = 1$mm or $s_{rel} = \pm 500\mu$m at an ambient pressure below $P_{amb} = 500$Pa. A position resolution of $res_{pos} < 50$nm is necessary to reach the target spectrometer resolution of $res_{target} = 10\text{cm}^{-1}$.

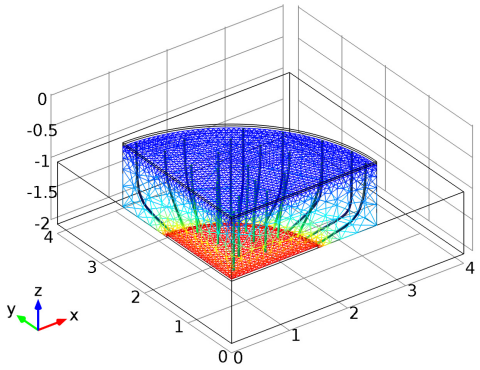

Fig. 3. Simplified illustration of the FEM simulation setup for the capacitive position sensor, axes are in mm.

B. Capacitive Sensor and Simulation

A micro-manufactured capacitive sensor is to be realized as multilayer structure, 1mm below the mirror plate (see Fig.1: Inkjet-printed sensor system). It comes with the advantage of a slim and readily integrable sensing solution, while providing high position resolution measurement capabilities (compare [23], [24]).

In the target capacitive sensor design, the bottom electrode is used as transmitter, and the mirror incorporates the receiver (see e.g. [25] for further explanation). Both are assumed to form a structure resembling a parallel plate capacitor. Which, in a simplifying approach, can be approximated by the following model

$$C = \frac{\epsilon_0 \epsilon_r A_r}{d} \tag{1}$$

where C is the capacitance in Farads, A_r the active plate area in square meters, ϵ_0 the dielectric constant of vacuum, ϵ_r the relative dielectric constant of the material between the plates and d the plate spacing in meters. Since Eq. 1 presents a simplistic approach mainly usable to aid a basic understanding of the system, accurate Finite Element Method (FEM) simulations (compare also [26]) are employed to consider all effective influences (e.g. fringing fields etc.). In Fig. 3 a simplified simulation setup is shown: The electrostatic field evolution is illustrated as coloured tubes emanating from the sensing electrode surface (red) and terminating at the mirror plane (blue). The mirror movement is incorporated by a moving mesh feature. The movement of the geometry is known, so the displacement of the mesh can be calculated at every time step using, e.g., a Laplace smoothing approach. For the Laplace smoothing, it is necessary to solve the partial differential equation

$$\frac{\partial^2 x}{\partial X^2} + \frac{\partial^2 y}{\partial Y^2} + \frac{\partial^2 z}{\partial Z^2} = 0 \tag{2}$$

The lowercase letters are deformed mesh positions and uppercase letters are the undeformed positions [27]. After the mesh

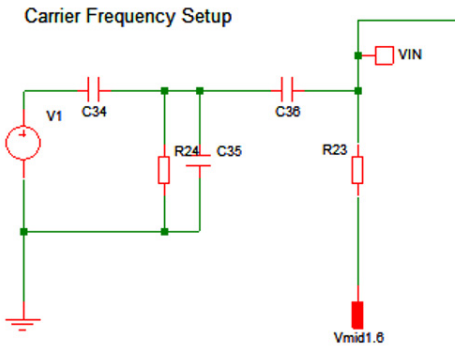

Fig. 4. Schematic illustration of the implemented carrier frequency setup.

deformation is determined, the electrostatics are computed by solving Gauss law

$$\nabla D = \rho_V \tag{3}$$

where the electric displacement field is

$$D = \epsilon_0 E \tag{4}$$

and ρ_V is the space charge density.

C. Analog Front-End

The analog front-end of the measurement system is composed of a carrier frequency setup (e.g. [28]) which connects to a specifically designed multistage Low Noise Amplifier (LNA) chain. The carrier frequency setup is illustrated in Fig. 4: C_{34} is the capacitance of interest (the position sensor) which, at the mirror rest position, is equal to the base capacitance C_b. R_{23} is the measurement shunt of $R_s = 50\Omega$. The value of the measurement shunt is chosen to match this circuit's impedance to the input impedance of $R_{23} = R_{in} = 50\Omega$. $C_{35} = C_p = 100$pF is the parasitic capacitance introduced by the conducting path to the input. $V1$ is the voltage source providing the excitation voltage $U_{exc} = 1$V at the carrier frequency $f_c = 20$MHz. $Vmid1.6$, the DC voltage source connected to R_{23}, is necessary to shift the input signal to the middle of the LNAs supply voltage. C_{36} is assembled to block DC offset voltages. Customized design of the LNA chain was necessary since commercially available hardware is not satisfying in terms of bandwidth and/or resolution. The chosen measurement system topology also provides a sufficient separation of the measurement and system drive frequencies. Thus, no disturbances of the mirror drive frequency will be seen at the much higher measurement frequency range.

D. Hardware Noise Analysis

In order to analyse the system capabilities in terms of uncertainty, it is necessary to determine basic noise figures as inflicted by the underlying electronics. Experimental characterization of the LNA chain yield a spectral input referred noise voltage of $U_n = 2.09\text{nV}/\sqrt{Hz}$ at the measurement shunt. The sensor base capacitance is found from FEM simulations to be $C_b = 109.3$fF. For further analyses, the capacitance equivalent noise $C_n = 0.151\text{aF}\sqrt{Hz}$ is necessary. It can be found from

$$C_n = \frac{U_n}{\frac{\partial U_{out}}{\partial C}} \tag{5}$$

as the ratio of the LNAs input referred noise voltage U_n and the system's output voltage sensitivity to capacitance changes. This sensitivity of the voltage at the shunt resistor with respect to variations in the capacitance is

$$\frac{\partial U_{out}}{\partial C} = \frac{U_{exc}}{8C_b^2 2\pi f_c (\frac{1}{R_s} + 8\pi C_p f_c)(\frac{1}{\frac{1}{R_s}+8\pi C_p f_c} + \frac{1}{8C_b \pi f_c})^2} \tag{6}$$

An expression for U_{out} can be found, using basic formulae for voltage divider circuits, as

$$U_{out} = \frac{U_{exc} Z_p}{Z_p + (\frac{1}{j2\pi f_c C_b})} \tag{7}$$

Here we use the measurement system's equivalent parallel impedance, which is

$$Z_p = \frac{1}{R_s + j2\pi f_c C_p} \tag{8}$$

with the parasitic parallel capacitance $C_p = 100$pF included. These equations are evaluated with a shunt resistor value $R_s = 50\Omega$, excitation voltage $U_{exc} = 1$V and carrier frequency $f_c = 20$MHz. We suggest the use of a calibration procedure to cope with variations in the base capacitance, uncertainties originating from topology deviations may then be neglected.

E. Sensor Model

In a first approach to a suitable semi-analytic model for the capacitive position sensor, a polynomial model is fitted to data from Finite Element Method (FEM) simulations. This is a commonly used process and well-documented in literature [12], [13].

We presume, the behaviour of the measured signal, i.e. the capacitance, $C(d_m)$ with d_m the parameter of interest, i.e. the mirror position, can be analytically described as (compare (1))

$$C(d_m) = \frac{\epsilon_0 \epsilon_r A_r}{d_m} \tag{9}$$

with the mirror position

$$d_m = d_0 + A_m cos(2\pi f_m t + \phi_m) \tag{10}$$

where $d_0 = 1$mm is the initial or rest position. $A_m = 0.5$mm is the absolute maximal displacement or amplitude, $f_m = 500$Hz the mirror resonance frequency and ϕ_m the mirror phase.

While the analytic description, as given above, is a simplistic version of the true system behaviour, simulation data provides an improved description. Hence, an analytic expression for this data is sought. Based on this expression, further resolution capability analyses of the considered system are possible. With respect to the given preconditions, it is a viable procedure to employ a Least Squares Estimator (LSE) (compare e.g. [29]). The resulting semi-analytic description (metamodel) of the simulation data is then used to quantify necessary conditions on the system bandwidth, noise and hardware parameters in order to provide the necessary position resolution.

TABLE I
UNCERTAINTIES FOR A PARAMETRIC SYSTEM DESCRIPTION

Parameter	Uncertainty	Unit
Amplitude	13·73	nm
Phase	$1{\cdot}1e^{-4}$	rad
Offset	$4{\cdot}034e^{-5}$	nm
Frequency	11·62	Hz

F. CRLB Analysis for the Parametric System

In Eq. 10, three parameters, i.e. phase ϕ_m, amplitude A_m and the frequency component f_m are supposed to be subject to environmental influences and thus time-varying. Under these assumptions, we can find the CRLB for the parameters, i.e. the lower bound of the variance, with respect to a chosen carrier frequency and bandwidth. The definition of the CRLB for a signal $s(\theta)$, dependent on the parameter of interest θ, is [29]

$$CRLB = \frac{\sigma^2}{\left(\frac{\partial s(\theta)}{\partial \theta}\right)^2} = \frac{\sigma^2}{\left(\frac{\partial C(d)}{\partial d}\right)^2} \tag{11}$$

The rightmost term is then the formulation adapted to our case. Analysing uncertainty evolution over bandwidth (Tab. I), restriction to $B = 2000$Hz is already yielding a theoretical lower bound of the uncertainty of $CRLB_A < 14$nm for the amplitude.

A direct measurement setup demands for intractable restrictions on the bandwidth, as we showed in [30]. We consequently suggest to employ a parametrized system model, exploiting prior knowledge. This enables us to adopt measurement strategies which allow to consider higher bandwidths. To realize such a strategy, we apply statistical methods, i.e. an EKF, which, in essence, is a Bayesian approach to signal reconstruction.

III. EXTENDED KALMAN FILTERING

Kalman filtering is a well-know estimation technique, used to recover signals from noisy measurements. Its applications range from robotics [31], pose estimation [32], sensorless control of synchronous drives [33], battery state of charge estimation for electric vehicles [34] to control of torsional micro-mirrors [35]. It is well-suited to solve problems where motion tracking of dynamic systems, which are either non-linear in their dynamics or in the measurement, is desired at the least computational expense.

A. Extended Kalman Filter Algorithm

The EKF is a suboptimal estimator based on Linear Minimum Mean Square Error (LMMSE) estimation and analytic linearisation (compare e.g. [36]). In terms of statistical signal processing, it is categorized as Bayesian approach. Expected mean values for the parameters of interest are assumed known a priori, as well as the system dynamics, and the measurement equation. These quantities and relations can be readily applied as initial conditions and modelling assumptions. Implementation of an optimal estimator calls for storage of the full probability density functions (e.g. [37]) describing the states. The Extended Kalman Filter, in contrast, can be implemented as recursive computation of the so-called sufficient statistic (see e.g. [29]). It subsequently yields the (approximate) mean and variance of the target system states. It is used for state prediction when the target system can be described by non-linear differential equations, or the measurement equation is non-linear, or both. For the interferometer system, only the measurement is described by a non-linear equation. In general, we assume a discrete time state space representation of the considered system which is of the form

$$\mathbf{x}_{k+1} = \boldsymbol{f}(\mathbf{x}_k) + \mathbf{v}_k$$

with $\boldsymbol{x}$ the system state, $\boldsymbol{f}$ the analytic description of the system dynamics and $\mathbf{v}$ is AWGN. The subscript indices here and in the following denote the respective time instances. The covariance matrix of the process noise is defined as

$$\boldsymbol{Q}_k = E\{\mathbf{v}_k \mathbf{v}_j^T\}$$

$E\{\cdot\}$ denotes the expectation operator. This matrix holds parameters, incorporating the necessary degrees of freedom to tune the control structure. We further fix the measurement to be

$$\mathbf{z}_k = h(\mathbf{x}_k) + \mathbf{w}_k$$

$h(\cdot)$ is the analytic description of the measurement function and $\mathbf{w}$ the measurement noise. The covariance matrix of the measurement noise is then defined as

$$\boldsymbol{R}_k = E\{\mathbf{w}_k \mathbf{w}_j^T\}$$

Additionally $\mathbf{v}$ and $\mathbf{w}$ are assumed uncorrelated. The system state incorporates a sufficient statistic accumulating all the information contained in previous states (under the assumption of AWGN). Consequently, the EKF yields the predicted state $\hat{\mathbf{x}}_k$, that is, the approximate conditional mean (if the AWGN assumption holds). The EKF also yields the associated covariance matrix $\boldsymbol{P}_k$, which, for the approximate conditional mean, is the matrix of the Mean Square Errors (MSEs). A flowchart illustrating the algorithm sequence is given in Fig. 5: In the first two steps of the Extended Kalman Filtering, the true as well as the predicted states are determined. The true state is subject to process noise as well as measurement noise. The predicted state is determined based on the system dynamics. Evaluating the measurement equation for the assumed system dynamics yields the predicted measurement. Then the covariance matrix is computed using the Jacobians of the system dynamics and the measurement equation. The difference of the predicted measurement and the true measurement is called residual. The residual is to be minimized in order for the EKF to represent the true system behaviour and output a more accurate state prediction. The covariance matrix is then necessary to determine the Kalman gain $\boldsymbol{k}$ which is the scaling parameter for the residual. Based on the Kalman gain and residual, the predicted state, as well as the covariance matrix, are corrected, and yield the new state prediction and covariance (i.e. MSE) matrix. Thus, the state estimated by the Kalman filter converges towards the true system behaviour, if adjusted correctly (through the process covariance matrix $\boldsymbol{Q}_k$).

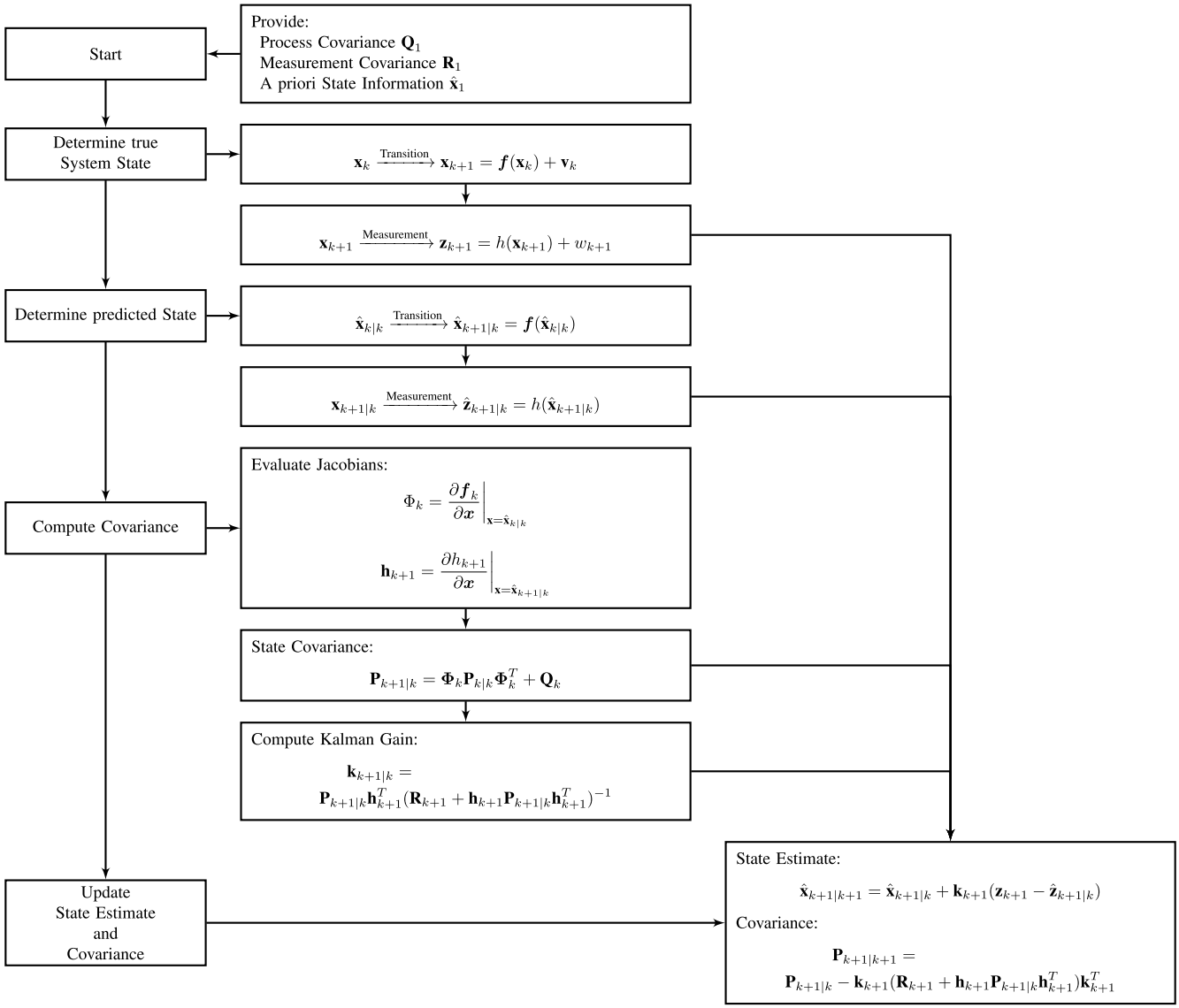

Fig. 5. Flowgraph for one iteration of extended Kalman filtering.

B. Process and Measurement Model

For the implementation of the EKF, as discussed in Sec. III-A, a discrete time state space representation of the target system is developed. The amplitude A_m, frequency f_m and phase ϕ_m of the MEMS-mirror are treated as state variables, we can thus define the state vector

$$\boldsymbol{x}_k = \begin{bmatrix} A_{m_k} & f_{m_k} & \phi_{m_k} \end{bmatrix}^T = \begin{bmatrix} x_{1_k} & x_{2_k} & x_{3_k} \end{bmatrix}^T \tag{12}$$

We apply the EKF to recover a sinusoidal mirror motion from noisy measurements (compare Eq. 10). Starting from the parametric description of the sinusoidal motion, we assume that amplitude and frequency stay constant from one time step to the next. This is reasonable since the MEMS mirror is a resonant system driven by a PWM of constant frequency. Furthermore, in the continuous case, we can express the angle of the target sinusoid as $\phi_m = 2\pi f_m t$, and its derivative with respect to time as $\dot{\phi} = 2\pi f_m$. Consequently, we can describe the angle $\phi_{m_{k+1}}$ as sum of the angle at time instant k, that is, ϕ_{m_k} and its discrete time equivalent derivative $\Delta\phi_m = 2\pi f_m t_s$. Here we add t_s as factor to account for the step width due to the chosen sampling time. We come to an analytic description of the system by denoting frequency and phase in state vector component notation:

$$\boldsymbol{f}(\boldsymbol{x}_k) = \begin{bmatrix} x_{1_k} & x_{2_k} & 2\pi t_s x_{2_k} + x_{3_k} \end{bmatrix}^T \tag{13}$$

The sensor model, i.e. the measurement equation based on simplistic assumptions (Eq. 1) can be given by

$$h(\boldsymbol{x}_k) = \epsilon_0 \epsilon_r \frac{A_r}{d(\boldsymbol{x}_k)} + w_k \tag{14}$$

$$\text{with } d(\boldsymbol{x}_k) = d_0 + x_{1_k} sin(2\pi t_s x_{2_k} + x_{3_k}) \tag{15}$$

To compute the Kalman gain $\boldsymbol{k}_k$ and the estimated covariance matrix $\boldsymbol{P}_k$, it is necessary to evaluate the Jacobians of the system dynamics and measurement equation with respect to the state vector at time instant k. $\boldsymbol{\Phi}_k$ is the Jacobian of the system dynamics (Eq. 13). Evaluated at $\boldsymbol{x}_k$, for the considered

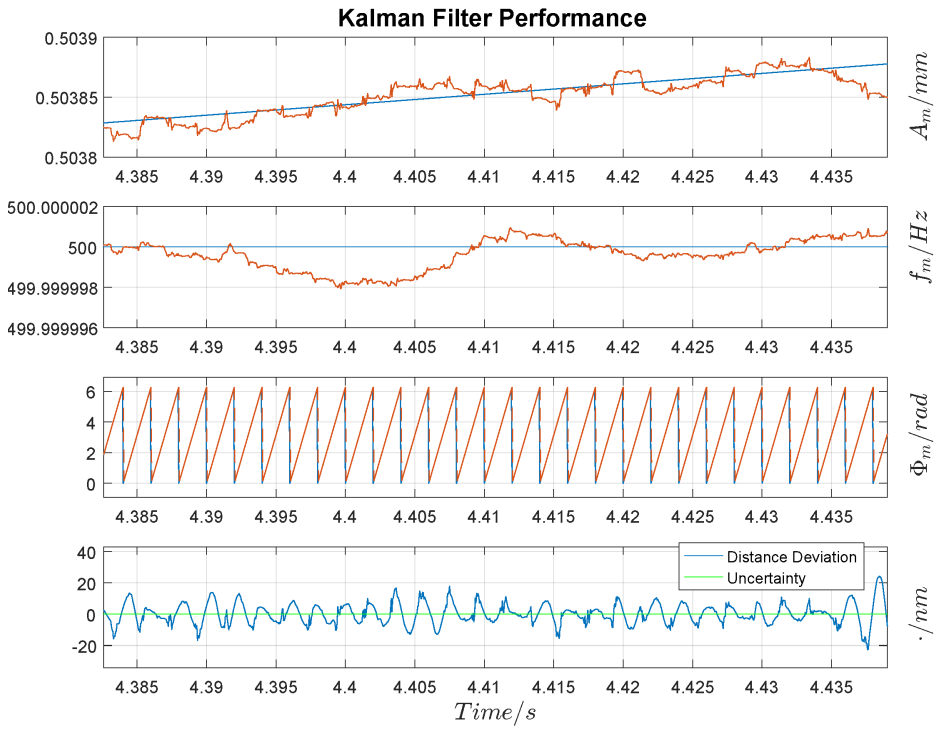

Fig. 6. Illustration of EKF performance metrics with an amplitude change rate of $r_{Amp} = 0.1\,\frac{\text{mm}}{\text{min}} = 20\,\frac{\%}{\text{min}}$ where the depicted view is already a zoom in of the performance as evaluated over the whole period of $t_{ev} = 6$s.

system, it is

$$\boldsymbol{\Phi}_k = \begin{bmatrix} 1 & 0 & 0 \\ 0 & 1 & 0 \\ 0 & 2\pi t_s & 1 \end{bmatrix}\Bigg|_k \tag{16}$$

$\boldsymbol{\Phi}_k$ is also called the transition matrix since it defines the transition relation (from one time step to the next). In our case, we could also drop the index for the time step because the transition matrix does not depend on the state vector (we work with a linear system description).

$\boldsymbol{H}_k$ is the Jacobian of the measurement equation (Eq. 14) evaluated at $\boldsymbol{x}_k$. It generally is a matrix, but since Eq. 14 is a scalar function, we are left with a row vector

$$\boldsymbol{h}_k = \begin{bmatrix} h_{k_1} & h_{k_2} & h_{k_3} \end{bmatrix}\Big|_k \tag{17}$$

where the individual components are

$$h_{k_1} = \frac{-\epsilon_0 \epsilon_r A_r sin(2\pi t_s x_{2_k} + x_{3_k})}{\left(d_0 + x_{1_k} sin(2\pi t_s x_{2_k} + x_{3_k})\right)^2} \tag{18}$$

$$h_{k_2} = 0 \tag{19}$$

$$h_{k_3} = \frac{-\epsilon_0 \epsilon_r A_r x_{1_k} cos(2\pi t_s x_{2_k} + x_{3_k})}{\left(d_0 + x_{1_k} sin(2\pi t_s x_{2_k} + x_{3_k})\right)^2} \tag{20}$$

Finally, we can describe the system trajectory, i.e. the evolution of the state from one time step to the next, in a discrete time state space form, as set of scalar equations

$$\begin{bmatrix} A_{m_{k+1}} \\ f_{m_{k+1}} \\ \phi_{m_{k+1}} \end{bmatrix} = \begin{bmatrix} 1 & 0 & 0 \\ 0 & 1 & 0 \\ 0 & 2\pi t_s & 1 \end{bmatrix} \begin{bmatrix} A_{m_k} \\ f_{m_k} \\ \phi_{m_k} \end{bmatrix} \tag{21}$$

Instead of using the analytic system description, the EKF is to be developed around the meta-model (compare Subsec. II-E) to incorporate the system behaviour more accurately.

IV. Results

In the suggested implementation of an EKF, we use amplitude A_m, frequency f_m and phase ϕ_m of the MEMS-mirror as state variables. System assessment is based on a sample run of the system together with the stochastic signal processing algorithm. The measurement noise C_n is determined as outlined in the Subsec. II-D on basic noise analysis. It is thus fixed for a specific bandwidth B and sampling frequency f_s. The measurement noise $\mathbf{w}$ and introduced systematic error e_{sys} will be the limiting factors for the filter performance in terms of position resolution res_{pos}. The measurement noise covariance $\boldsymbol{R}$ is dependent on the sampling frequency f_s, with higher sampling frequency leading to an increased noise figure. On the other hand, the higher sampling frequency calls for a reduced process noise covariance matrix $\boldsymbol{Q}$ (amplitudes of changes between sample points will decrease). With a concise sampling strategy applied, these terms should ideally cancel each other. Thus, higher sampling frequencies are allowed with only little alteration on the achieved resolution.

Samplewise evaluations of the EKF performance under the described assumptions, and an amplitude change rate (which essentially is the systematic error e_{sys}) of $r_{amp} = 0.1\frac{\text{mm}}{\text{min}} = 20\frac{\%}{\text{min}}$, indicate well sufficient resolution capabilities of $res_{pos} \approx 20$nm. The result is given in Fig. 6 and the plots are described from top to bottom: The sampling rate is fixed to $f_s \approx 194$kHz. The uppermost plot depicts the true amplitude (blue) and the estimated amplitude (red, dashed). In the second plot, the true (blue) and the estimated (red, dashed) frequency are compared. Estimated and true phase (which is between $\phi_{min} = 0$rad and $\phi_{max} = 2\pi$rad) follow in the third plot. The deviation between estimated and true

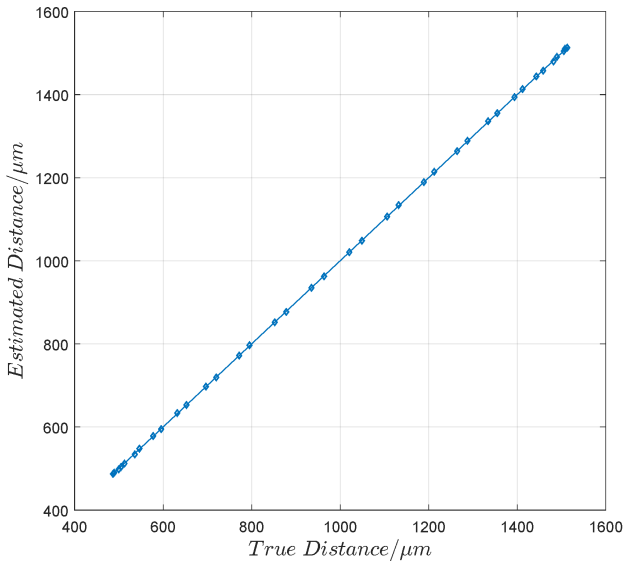

Fig. 7. Illustration of estimated distance over true distance.

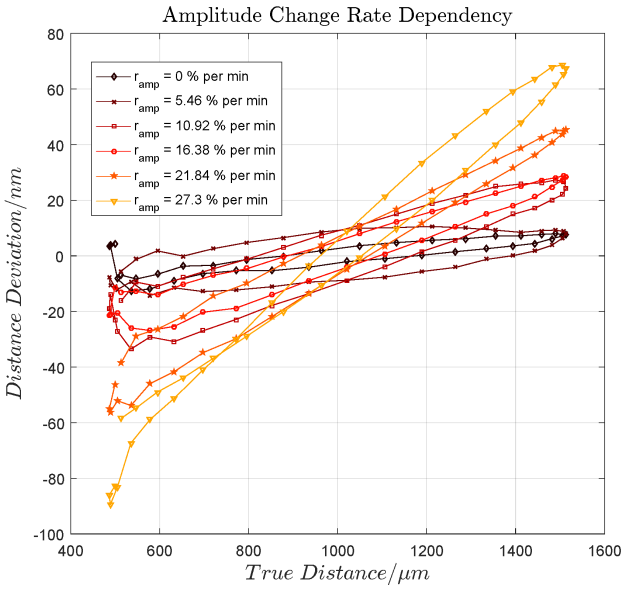

Fig. 8. Illustration of the effect of various amplitude change rates on the distance error (coloured ellipses) with the sampling frequency fixed to $f_s \approx$ 194kHz.

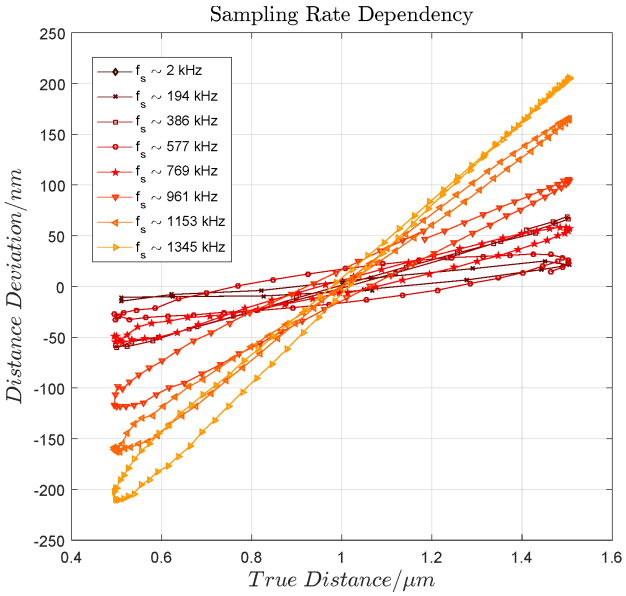

Fig. 9. Illustration of how different sampling frequencies affect the distance resolution, considering also an amplitude change rate of $r_{Amp} = 0.1\,\frac{\text{mm}}{\text{min}} = 20\,\frac{\%}{\text{min}}$.

trajectories of amplitude, frequency and phase are marginal, but still influence the estimation process to result in a deviation of $d_{err} \approx$ 20nm. This deviation is depicted in the fourth plot. This lowermost graph also gives the estimated absolute amplitude uncertainty (green, rather linear evolution): this is the covariance of the amplitude as estimated by the filter and is in the range of $unc_{Amp} =$ 2nm. Such a value can only be reached without systematic deviations (i.e. without or with slow amplitude variation). Temperature influence is assumed to cause deviations of mechanical mirror properties and unstable vacuum conditions are leading to varying amplitudes when driven with a constant PWM signal. The amplitude variation, a systematic error, is investigated to prove suitability of the chosen signal processing under such conditions. Additionally, the system behaviour with different amplitude change rates from $r_{amp} =$ 0–0.15 $\frac{\text{mm}}{\text{min}}$, i.e. a maximum of $r_{amp} \approx 30\frac{\%}{\text{min}}$ relative variation, were considered.In Fig. 7 we see a linear relationship of the estimated (d_{est}) and true distance (d_{true}). The error $d_{err} = d_{true} - d_{est}$ (coloured curves in Fig. 8) evolves in a non-linear fashion with values between $d_{err} =$ 0nm for no amplitude change up to $d_{err} \approx$ 60nm for a deviation of $r_{amp} \approx 27\frac{\%}{\text{min}}$. In this case, the distance error d_{err} is equivalent to the smallest detectable position change, and is thus the same as the position resolution res_{pos} of the capacitive sensor. Its evolution is quasi-symmetric for negative and positive relative mirror-movement. The error is largest at the mirror's turning points which are located at $d_{min} = 500\mu$m, and $d_{max} = 1500\mu$m respectively. The influence of the sampling frequency was investigated alongside (see Fig. 9). For varying sampling frequencies, an increase in the measurement noise results, which then causes a lowered achievable resolution. Although the true systematic deviation is expected to be below this value, investigations were done employing a fixed amplitude variation of $r_{amp} = 20\frac{\%}{\text{min}}$. With these changed conditions, we see a reduced resolution $res_{pos} <$ 200nm with application of sampling frequencies in the range of $f_s \approx$ 1.4MHz. The position resolution decreases, but this decrease is not significant compared to the resolution loss using a different measurement strategy and such an increased bandwidth.

In the preliminary analysis in Subsec. II-F, the theoretically achievable lower bounds on the system uncertainty were determined. These theoretical bounds are not achievable by the EKF in this setup, since systematic error (amplitude variation) is considered as well. The CRLB is only achievable with an idealized EKF when the covariance propagation equations are linearized about the true, yet unknown trajectory [38]. While our experiments were done assuming an amplitude variation, the EKF will reach the lower bound for static systems subject to only AWGN.

V. Conclusion

First, the considered MEMS-mirror as part of a Michelson interferometer and the suggested inkjet-printed capacitive position sensor, measurement system and respective noise analysis were presented. Hardware noise analysis based on the developed analog front-end for capacitive position sensing was elaborated. The considered measurement system is ready for multifunctional purposes, i.e. different sensors and measurement strategies, and it is further integrable into a miniaturised device package. Noise analysis is used for assessment of the CRLB of a parametric system description,to attain the CRLB was shown to be only theoretically feasible in the considered setup. An EKF was developed and realized for mirror position tracking to cope with systematic errors and changing sampling rates, i.e. changing bandwidth requirements. The capabilities of this Bayesian signal processing approach were analysed and illustrated based on simulations of the system. The major reduce of influence of the sampling frequency on the system resolution was demonstrated. In general, capacitive position sensing is not feasible when a direct measurement strategy is employed. Resorting to a parametric system description in combination with stochastic signal processing can present a way out. Through this analysis, we demonstrate the usability of generally sub-optimal sensing structures by adoption of suitable signal-processing algorithms.

References

[1] A. Tortschanoff, A. Kenda, M. Kraft, T. Sandner, H. Schenk, and W. Scherf, "Improved MOEMS-based ultra-rapid Fourier transform infrared spectrometer," *Proc. SPIE*, vol. 7319, p. 73190I, Apr. 2009.

[2] A. D. Yalcinkaya, H. Urey, D. Brown, T. Montague, and R. Sprague, "Two-axis electromagnetic microscanner for high resolution displays," *J. Microelectromech. Syst.*, vol. 15, no. 4, pp. 786–794, Aug. 2006.

[3] C. Winter *et al.*, "Micro-beamer based on MEMS micro-mirrors and laser light source," *Procedia Chem.*, vol. 1, pp. 1311–1314, Sep. 2006.

[4] A. Kenda *et al.*, "MOEMS-based scanning light barrier," *Procedia Chem.*, no. 1, no. 1, pp. 1299–1302, 2009.

[5] A. P. Lee, C. F. McConaghy, G. Sommargren, P. Krulevitch, and E. W. Campbell, "Vertical-actuated electrostatic comb drive with *in situ* capacitive position correction for application in phase shifting diffraction interferometry," *J. Microelectromech. Syst.*, vol. 12, no. 6, pp. 960–971, Dec. 2003.

[6] A. Tortschanoff, M. Lenzhofer, A. Frank, A. Kenda, T. Sandner, and H. Schenk, "Improved MEMS based FT-IR spectrometer," in *Proc. IEEE Int. Symp. Optomechatron. Technol.*, Sep. 2009, pp. 116–121.

[7] M. Lenzhofer *et al.*, "Position encoding and closed loop control of MOEMS translatory actuators," *Proc. SPIE*, vol. 7362, p. 736212, May 2009.

[8] A. Tortschanoff, M. Baumgart, D. Holzmann, M. Lenzhofer, T. Sandner, and A. Kenda, "Compact optical position feedback scheme for MOEMS mirrors," *Microsyst. Technol.*, vol. 20, no. 4, pp. 743–749, Apr. 2014.

[9] V. Annovazzi-Lodi, S. Merlo, and M. Norgia, "Comparison of capacitive and feedback-interferometric measurements on MEMS," *J. Microelectromech. Syst.*, vol. 10, no. 3, pp. 327–335, Sep. 2001.

[10] V. F.-G. Tseng, L. Wu, and H. Xie, "Inductive eddy current sensing as a displacement sensing mechanism for large piston/rotation micromirrors," in *Proc. IEEE Transducers*, Jun. 2015, pp. 176–179.

[11] J.-I. Lee, X. Huang, and P. Chu, "Nanoprecision MEMS capacitive sensor for linear and rotational positioning," *J. Microelectromech. Syst.*, vol. 18, no. 3, pp. 660–670, Jun. 2009.

[12] A. J. Fleming, "A review of nanometer resolution position sensors: Operation and performance," *Sens. Actuators A, Phys.*, vol. 190, pp. 106–126, Feb. 2013.

[13] T. R. Hicks and P. D. Atherton, *The NanoPositioning Book*. Torquay, U.K.: Queensgate Instruments Limited, 1997.

[14] S. I. Moore and S. O. R. Moheimani, "Displacement measurement with a self-sensing MEMS electrostatic drive," *J. Microelectromech. Syst.*, vol. 23, no. 3, pp. 511–513, Jun. 2014.

[15] M. S.-C. Lu and G. K. Fedder, "Position control of parallel-plate microactuators for probe-based data storage," *J. Microelectromech. Syst.*, vol. 13, no. 5, pp. 759–769, Oct. 2004.

[16] B. Cagdaser and B. E. Boser, "Low-voltage electrostatic actuation with inherent position feedback," *J. Microelectromech. Syst.*, vol. 21, no. 5, pp. 1187–1196, Oct. 2012.

[17] A. Mawardi and R. Pitchumani, "Design of microresonators under uncertainty," *J. Microelectromech. Syst.*, vol. 14, no. 1, pp. 63–69, Feb. 2005.

[18] J. W. Wittwer, M. S. Baker, and L. L. Howell, "Robust design and model validation of nonlinear compliant micromechanisms," *J. Microelectromech. Syst.*, vol. 15, no. 1, pp. 33–41, Feb. 2006.

[19] G. Zhu, J. Levine, L. Praly, and Y. A. Peter, "Flatness-based control of electrostatically actuated MEMS with application to adaptive optics: A simulation study," *J. Microelectromech. Syst.*, vol. 15, no. 5, pp. 1165–1174, Oct. 2006.

[20] B. C. Smith, *Fundamentals of Fourier Transform Infrared Spectroscopy*. Boca Raton, FL, USA: CRC Press, 2011.

[21] A. Kenda *et al.*, "Development, characterization and application of compact spectrometers based on MEMS with in-plane capacitive drives," *Proc. SPIE*, vol. 9101, p. 910102, May 2014.

[22] A. Kenda, C. Drabe, H. Schenk, A. Frank, M. Lenzhofer, and W. Scherf, "Application of a micromachined translatory actuator to an optical FTIR spectrometer," *Proc. SPIE*, vol. 6186, p. 618609, Apr. 2006.

[23] M. Carminati, G. Ferrari, F. Guagliardo, and M. Sampietro, "ZeptoFarad capacitance detection with a miniaturized CMOS current front-end for nanoscale sensors," *Sens. Actuators A, Phys.*, vol. 172, pp. 117–123, Dec. 2011.

[24] T. Zeng *et al.*, "A capacitive sensor for the measurement of departure from the vertical movement," *IEEE Trans. Instrum. Meas.*, vol. 65, no. 2, pp. 458–466, Feb. 2016.

[25] L. K. Baxter, *Capacitive Sensors: Design and Applications*. Piscataway, NJ, USA: IEEE Press, 1997.

[26] L.-M. Faller and H. Zangl, "Robust design of a 3D- and inkjet-printed capacitive force/pressure sensor," in *Proc. IEEE EuroSimE*, Apr. 2016, pp. 1–7.

[27] *Comsol Multiphysics Documentation, Version 5.2*, Comsol Multiphysics GmbH, Berlin, Germany, Feb. 2016.

[28] H. Zangl, "Design paradigms for robust capacitive sensors," Ph.D. dissertation, Dept. Inst. Elect. Measurement Signal Process., Graz Univ. Technol., Graz, Austria, 2005.

[29] S. M. Kay, *Fundamentals of Statistical Signal Processing: Estimation Theory*. Englewood Cliffs, NJ, USA: Prentice-Hall, 1993.

[30] L.-M. Faller and H. Zangl, "Towards feasibility of an inkjet-printed capacitive sensor for position tracking of a MOEMS-mirror in a Michelson interferometer setup," in *Proc. Eurosensors*, 2016, pp. 912–915.

[31] S. Cruz, D. M. Muñoz, M. Conde, C. H. Llanos, and G. A. Borges, "FPGA implementation of a sequential extended Kalman filter algorithm applied to mobile robotics localization problem," in *Proc. IEEE 4th Latin Amer. Symp. Circuits Syst. (LASCAS)*, Feb./Mar. 2013, pp. 1–4.

[32] G. Ligorio and A. M. Sabatini, "Extended Kalman filter-based methods for pose estimation using visual, inertial and magnetic sensors: Comparative analysis and performance evaluation," *Sensors*, vol. 13, no. 2, pp. 1919–1941, 2013.

[33] L. Idkhajine, E. Monmasson, and A. Maalouf, "Fully FPGA-based sensorless control for synchronous AC drive using an extended Kalman filter," *IEEE Trans. Ind. Electron.*, vol. 59, no. 10, pp. 3908–3918, Oct. 2012.

[34] C. Jiang, A. Taylor, C. Duan, and K. Bai, "Extended Kalman filter based battery state of charge(SOC) estimation for electric vehicles," in *Proc. IEEE Transp. Electrific. Conf. Expo (ITEC)*, Jun. 2013, pp. 1–5.

[35] C.-G. Agudelo, G. Zhu, M. Packirisamy, and L. Saydy, "Flatness-based control of an electrostatic torsional micro-mirror with voltage feedback," in *Proc. 50th Midwest Symp. Circuits Syst.*, Aug. 2007, pp. 654–657.

[36] Y. Bar-Shalom, X. R. Li, and T. Kirubarajan, *Estimation With Applications to Tracking and Navigation*. Hoboken, NJ, USA: Wiley, 2001.

[37] F. van der Heijden, R. P. Duin, D. de Ridder, and D. M. Tax, *Classification, Parameter Estimation and State Estimation*. Hoboken, NJ, USA: Wiley, 2004.

[38] J. Taylor, "The Cramer–Rao estimation error lower bound computation for deterministic nonlinear systems," in *Proc. IEEE Conf. Dec. Control Including 17th Symp. Adapt. Process.*, Jan. 1978, pp. 1178–1181.

Lisa-Marie Faller received the B.Sc. degree in systems engineering and the M.Sc. degree in systems design from the Carinthia University of Applied Sciences (CUAS), Villach, Austria, in 2011 and 2014, respectively. She is currently pursuing the Ph.D. degree in inkjet-printed capacitive sensing system for a MEMS micro-mirror as part of an infrared-spectrometer. During her master's, she was at the Integrated Systems and Circuits Research Group, CUAS, where she was involved in the design of colour sensors fabricated in CMOS technology. In 2014, she joined the Sensors and Actuators Institute of Smart System Technologies, Alpen-Adria-Universität Klagenfurt, Austria, where she was involved in robust design and statistical signal processing and was a Research and Teaching Assistant.

Hubert Zangl received the Dipl.Ing. degree in telematics, the Dr.Tech. degree in electrical engineering, and the Venia Docendi degree in sensors and instrumentation from the Graz University of Technology (TUG), Graz, Austria, in 2001, 2005, and 2009, respectively. From 2010 to 2013, he was an Associate Professor of sensors and instrumentation at the Institute of Electrical Measurement and Measurement Signal Processing, TUG. Since 2013, he has been a Professor chairing sensors and actuators with the Institute of Smart System Technologies, Alpen-Adria-Universität Klagenfurt, Austria. He has authored or co-authored over 100 international scientific publications, and holds several patents. His research interests include the design and optimization of smart sensors and actuators, robustness and reliability of sensors and actuators, sensor signal processing, autarkic wireless sensors, and energy harvesting.